

2001

# Mapping Abyssal Current and Pressure Fields under the Meandering Gulf Stream

D. Randolph Watts

*University of Rhode Island*, randywatts@uri.edu

Xiaoshu Qian

*See next page for additional authors*

Follow this and additional works at: <https://digitalcommons.uri.edu/gsofacpubs>

---

## Citation/Publisher Attribution

Watts, D. R., Qian, X., & Tracey, K. L. (2001). Mapping Abyssal Current and Pressure Fields under the Meandering Gulf Stream. *Journal of Atmospheric and Oceanic Technology*, 18, 1052-1067. doi: 10.1175/1520-0426(2001)0182.0.CO;2  
Available at: [https://doi.org/10.1175/1520-0426\(2001\)0182.0.CO;2](https://doi.org/10.1175/1520-0426(2001)0182.0.CO;2)

This Article is brought to you for free and open access by the Graduate School of Oceanography at DigitalCommons@URI. It has been accepted for inclusion in Graduate School of Oceanography Faculty Publications by an authorized administrator of DigitalCommons@URI. For more information, please contact [digitalcommons@etal.uri.edu](mailto:digitalcommons@etal.uri.edu).

---

**Authors**

D. Randolph Watts, Xiaoshu Qian, and Karen L. Tracey

## Mapping Abyssal Current and Pressure Fields under the Meandering Gulf Stream

D. RANDOLPH WATTS, XIAOSHU QIAN,\* AND KAREN L. TRACEY

*Graduate School of Oceanography, University of Rhode Island, Narragansett, Rhode Island*

(Manuscript received 20 March 2000, in final form 25 September 2000)

### ABSTRACT

Using bottom pressure measurements and current meter measurements at 3500-m depth at 12 sites under the Gulf Stream near 68°W daily optimally interpolated (OI) maps have been constructed for June 1988 to August 1990. Prior to mapping, the pressure records were leveled (referenced to the same absolute geopotential) using the current measurements under the assumption that their mean fields are geostrophic. The leveled pressures were subsequently used together with the current measurements in a multivariate, nondivergent OI mapping procedure. This procedure significantly reduced the mapping errors, because both pressure and its (geostrophic) gradient are specified as inputs. The mapped bottom pressure and current fields have typical mean-square errors of only 0.0005 db<sup>2</sup> and 4 cm<sup>2</sup> s<sup>-2</sup>, compared to typical signal variances of 0.0035 db<sup>2</sup> and 80 cm<sup>2</sup> s<sup>-2</sup>. The daily maps of abyssal pressure are used to identify the characteristic space–time structures of dynamical processes. Examples are shown in which deep-level cyclones spin up jointly with steep stationary troughs in the Gulf Stream and deep anticyclones with steep propagating crests. Another sequence of maps illustrates the propagation of topographic Rossby waves and ring–stream interactions.

### 1. Introduction

For decades meteorologists have employed barometers to chart atmospheric pressure in the study of synoptic weather systems, but physical oceanographers have lacked the equivalent routinely available tool for deep-sea studies. In the deep ocean, ambient pressures may typically be 4000 db or more (1 db = 10 kPa) and yet the desired subtidal dynamic pressure signals may be less than 0.08 db (approximately the same size as for atmospheric pressure signals). Thus, the sensor requirements are stringent—the measurements must be stable to within a few parts per million (ppm). The measurement of pressure in the deep ocean for dynamic studies is intrinsically much more difficult than in the atmosphere, for two principal reasons: leveling and drift.

“Leveling,” the technique of referring all measurements onto a geopotential surface, is difficult in seawater (about 1000 times denser than air) because hydrostatic pressure changes about 1 db per meter depth. Leveling in the abyssal ocean to the desired centimeter-accuracy is not yet attained by direct depth measurement (surveying). Consequently, for some purposes no leveling is attempted; instead an arbitrary reference pressure

(such as the mean) is sometimes removed from a record, and only the temporal variability studied. In this study, leveling of the measured pressures was accomplished by also measuring the abyssal currents and assuming their *mean* fields are geostrophic.

Interestingly, the absolute calibration accuracy (typically 0.01%, or 0.4 db) of the pressure sensors is not a stringent requirement, because depth uncertainties are usually greater: the instrument depth may be uncertain by more than 1 m relative to the geoid. Hence, both the absolute calibration and depth uncertainties are compensated by leveling.

“Drift” refers to a temporal change in pressure calibration. To study synoptic or mesoscale variability, it is desirable that the sensor, once leveled, not drift more than 0.01 db during the deployment period—a fraction of the desired dynamic signal—and that the drift be slow compared to the eddy signal.

Considerable effort has gone into developing low-drift deep-sea pressure sensors (Filloux 1970, 1980; Baker 1981). Using sensors developed by Paros (1976) and Wearn and Larson (1982), Watts and Kontoyiannis (1990; hereafter referred to as WK90) report methods (a) to reduce drift by preconditioning the sensors and (b) to fit and remove any remaining drift so that the residual records drift less than 0.02 db in a year. In this study, the WK90 techniques were applied to improved model (Bourdon tube activated) Digiquartz sensors and yielded residual records with drifts of less than 0.01 db in most cases.

This paper documents the main steps of our obser-

\* Current affiliation: Intel Corporation, San Jose, California.

*Corresponding author address:* Dr. D. Randolph Watts, Graduate School of Oceanography, University of Rhode Island, South Ferry Road, Narragansett, RI 02882.  
E-mail: rwatts@gso.uri.edu

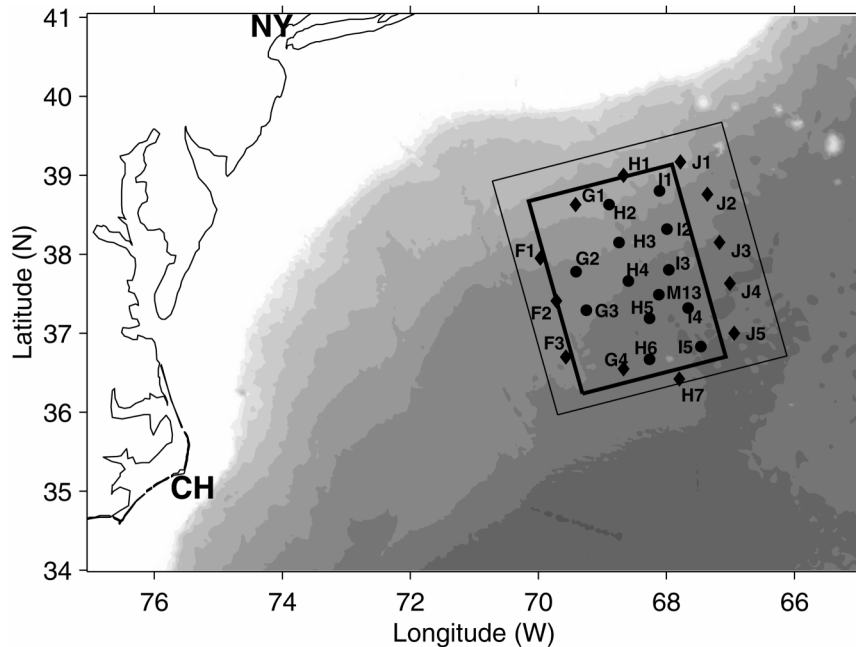


FIG. 1. Moored instrumentation in the SYNOP central array. Solid circles indicate sites with both current meter moorings and PIESs (except M13, which did not have a PIES). Solid diamonds designated sites with only IESs. The smaller box, outlined by the bold line, indicates the region mapped by the multivariate OI procedure described herein. The larger box indicates the thermocline depth mapping region. Bathymetry is shaded at 500-m intervals. Cape Hatteras and New York are labeled for reference.

vational procedures: 1) drift avoidance and removal in the pressure records; 2) determining the reference pressures to level the records; and 3) mapping the daily fields of  $P$ ,  $u$ , and  $v$ . The latter two steps both utilize optimal interpolation (OI), in which the currents and pressure are dynamically constrained by the covariance functions to be geostrophically related. The subsequent sections verify the accuracy of the output ( $P$ ,  $u$ ,  $v$ ) maps, and give examples of the abyssal eddy fields that were observed. The maps revealed that the abyssal field was organized into cyclonic and anticyclonic circulations in which the currents grew as strong as  $45 \text{ cm s}^{-1}$ . Being essentially depth-independent (Savidge and Bane 1999a) these eddies have important dynamical implications for the upper-layer jet as well as for abyssal levels. These dynamical implications are investigated in other works, which use the mapped fields at 3500 m to study the four-dimensional structure, kinematics, dynamics, and energetics of Gulf Stream meanders (Kim 1994; Lindstrom and Watts 1994; Shay et al. 1995; Watts et al. 1995; Cronin and Watts 1996; Lindstrom et al. 1997; Savidge and Bane 1999a,b).

## 2. Data

The data for this study come from pressure recorders on the ocean bottom and current meters on the 3500-m depth horizon. The instruments were deployed as part of the Synoptic Ocean Prediction experiment (SYNOP

Central Array, under a strongly meandering region of the Gulf Stream centered near  $68^\circ\text{W}$ . The pressure sensors were on inverted echo sounders (PIES) at 12 sites and nearby were 13 current meter (CM) moorings, arranged as in Fig. 1. The instrument spacings were designed to study steep meanders in the Gulf Stream. The instruments were 50–60 km apart and spanned about 280 km cross-stream by 200 km alongstream. The data were collected between June 1988 and August 1990. All PIES records were detided by the Munk and Cartwright (1966) response analysis, and all pressure and current ( $P$ ,  $u$ ,  $v$ ) time series were 40-h low-pass filtered. Details of the SYNOP moored array design and measurements are given in Watts et al. (1995) and Shay et al. (1995).

## 3. Pressure sensor preconditioning and drift removal

The pressure sensors were Digiquartz 6000-psi range transducers manufactured by Paroscientific, Inc. (Paros 1976; Wearn and Larson 1982). The sensing element is a quartz crystal double-ended tuning fork resonator, the frequency of which changes in response to a stress load applied by a Bourdon tube. Instrumental details are provided in WK90, including a schematic drawing of the sensing elements. Here, we provide information only on changes since WK90.

Since WK90 found that preconditioning significantly reduced sensor drift in the earlier model Bellows-acti-

vated sensors, we felt that preconditioning could also be beneficial to the Bourdon-tube-activated sensors. Thus, all sensors were preconditioned to deep pressures to minimize drifting. The older sensors were preconditioned by deployment at similar depths during a prior field program and the newly purchased sensors were subjected to pressures of 3000–4000 db for 1–2 months in the lab. During the present experiment, drift in year-long records was undetectable at 10 of 22 sites. For the remaining 12 records, the drifts, which exceeded  $0.02 \text{ db yr}^{-1}$ , were estimated and removed as follows.

These observed drifts might have arisen from drifting of the time base clock within the PIES. The frequency-counting, time-interval determination by the clock is required to have less than one-tenth the drift of the pressure sensors, for which the frequency changes by only 10% at full-scale pressure. Following the findings reported in WK90 the time base clock crystal specification was upgraded to 0.5 ppm drift per year for this experiment. Despite these precautions, in several of the instruments the clock frequency had a constant offset of about 10 ppm because, as we later discovered, the laboratory-standard frequency counter was out of calibration. The effect was to introduce a 100 ppm constant offset in the pressure, which appeared as a minimally bothersome hydrostatic error. Despite the clock upgrade, we cannot definitively state whether the detectable pressure drifts ( $>5 \text{ ppm}$ ) in the 12 records were attributable to clock crystal drift or to pressure sensor drift.

To remove the drift from the 12 records, we applied the techniques that WK90 reported to work best for these sensors: an exponential-plus-linear drift curve was determined by least squares fit and then subtracted from the measurements. WK90 showed that this fit outperformed both log and power-law-fitted curves. Low-frequency ocean variability may be removed by this procedure.

Altogether, we estimate that (after dedrifting the above 12) the 22 pressure records used in this paper have residual drifts of no more than 0.015 db in their year-long records. Pressure time series plots can be found in Fields and Watts (1990 and 1991) and Qian and Watts (1992).

#### 4. Leveling and mapping

Accurate maps of the daily pressure and current fields were obtained by combining the leveled pressure measurements and current measurements in a multivariate, nondivergent optimal interpolation (OI) procedure. Maps of the streamfunction field  $p$  could have been generated from  $(u, v)$  current measurements alone. The resulting maps would have been spatially consistent since the current measurements were spaced close enough to be well correlated. However, each daily map would have had a different, undetermined reference level. In other words, they would be temporally inconsistent by an amount comparable to the eddy signals. This

is physically reasonable, since  $p$  maps generated (as streamfunctions) solely from velocity measurements stem from only the measured gradients of pressure. On the other hand, the dedrifted pressure  $P'$  records from bottom pressure sensors are temporally consistent. Yet by themselves, they are not suitable inputs for OI mapping until they have been leveled, because each site has an arbitrary level (or reference pressure) relative to the others, that is, they would be spatially inconsistent. Once leveled, the pressures alone could have been used to produce spatially and temporally consistent maps. However, by combining them with the measured currents in a multivariate mapping procedure more accurate mapped fields were produced. Reduced mapping errors were obtained because pressure as well as its gradients were supplied to the mapping procedure. Furthermore, by our choice of covariance functions, the output fields  $(P, u, v)$  were constrained to be geostrophic (Bretherton et al. 1976).

##### a. Leveling

Leveling was accomplished by assuming that the measured *mean* abyssal currents were geostrophic and determining the reference pressures accordingly. Additional assumptions are implied in combining the dedrifted  $P, u, v$  data for leveling. (a) The dynamic pressure at the ocean bottom does not change from its geostrophic values (other than hydrostatically) just above the bottom boundary layer, an assumption that is well justified theoretically (Pedlosky 1987). (b) The vertical shear (thermal wind) of the currents is small at the 3500-m level, as is observed from the smallness of lateral gradients of density, so that horizontal pressure gradients measured near the bottom are the same as at 3500 m.

The leveling procedure is diagrammed at the top of the flowchart in Fig. 2. The OI technique was applied on the current measurements alone to map the streamfunction ( $p$ ) fields (the process is designated as “u2p” in the upper-right corner). The interpolation of these streamfunction fields to the sites of the PIES instruments yielded a set of pressure time series, each with an offset that is only time dependent (spatially uniform). Let  $p(t, s)$  and  $p_0(t)$  denote at site  $s$  this optimally interpolated pressure time series and its time-dependent unknown offset from the absolute pressure. Let  $P'(t, s)$  and  $P_0(s)$  represent at site  $s$  the measured (dedrifted) pressure and its site-dependent unknown reference level (temporally constant). Since the absolute pressure at a given time and site is unique,

$$P'(t, s) + P_0(s) = p(t, s) + p_0(t).$$

The unknown  $p_0(t)$  may be eliminated by subtracting the above equation for any one site (we used site G2) from the equations for all other sites, giving

$$\Delta_s P_0(s) = \Delta_s p(t, s) - \Delta_s P'(t, s), \quad (1)$$

where  $\Delta_s$  is the spatial difference operator. The left-hand

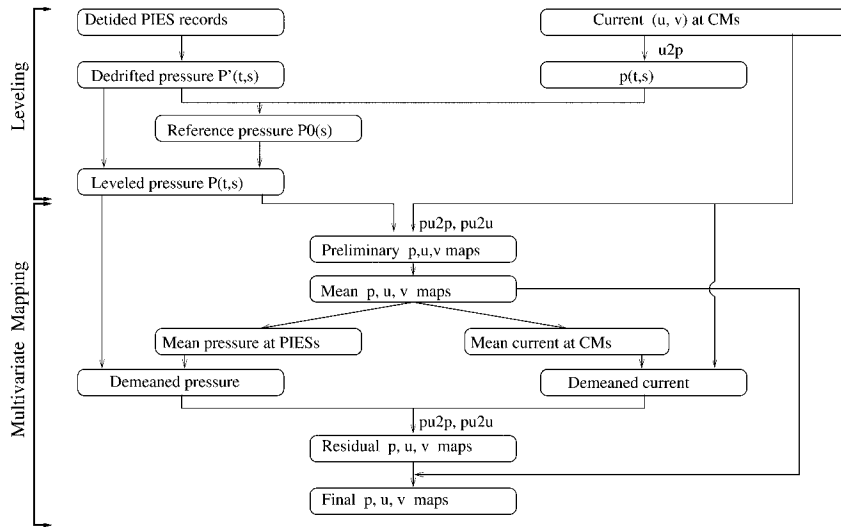


FIG. 2. Data processing flowchart. Variables and program steps are as in text.

term is independent of time. However, the right-hand side, estimated from real data, varies with time due to errors primarily arising from mapping  $p(t, s)$  each day. Changes in  $P(t, s)$  between 3500 m and the ocean bottom associated with nonzero vertical shear above each PIES may possibly contribute to the error as well. Therefore, for each site the reference level on the left-hand side

was calculated as the time average of the right-hand side where the averaging period is the overlapping time of good pressure data between site  $s$  and site G2. If the measurement periods for all sites were identical the last term in Eq. (1) would average to zero, and the above procedure would simplify to applying nondivergent OI on the mean current records to estimate the mean

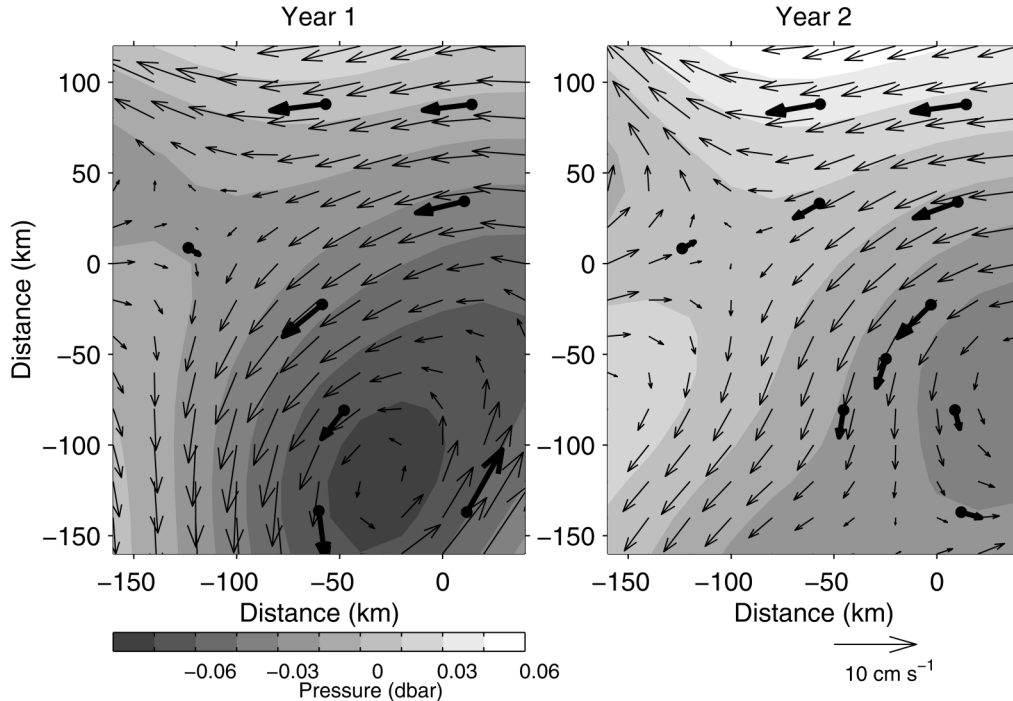


FIG. 3. One-year averages of the multivariate-OI mapped bottom pressure and current fields with the mean measured currents superimposed (bold vectors). Year 1 is 16 Jun 1988–24 May 1989, and year 2 is 29 Aug 1989–7 Aug 1990. Solid circles indicate only the sites for which the mean currents could be determined. The frames correspond to the smaller boxed region in Fig. 1. Distances are calculated from the origin at 38°N, 68°W, and the x axis is oriented along 075° true.



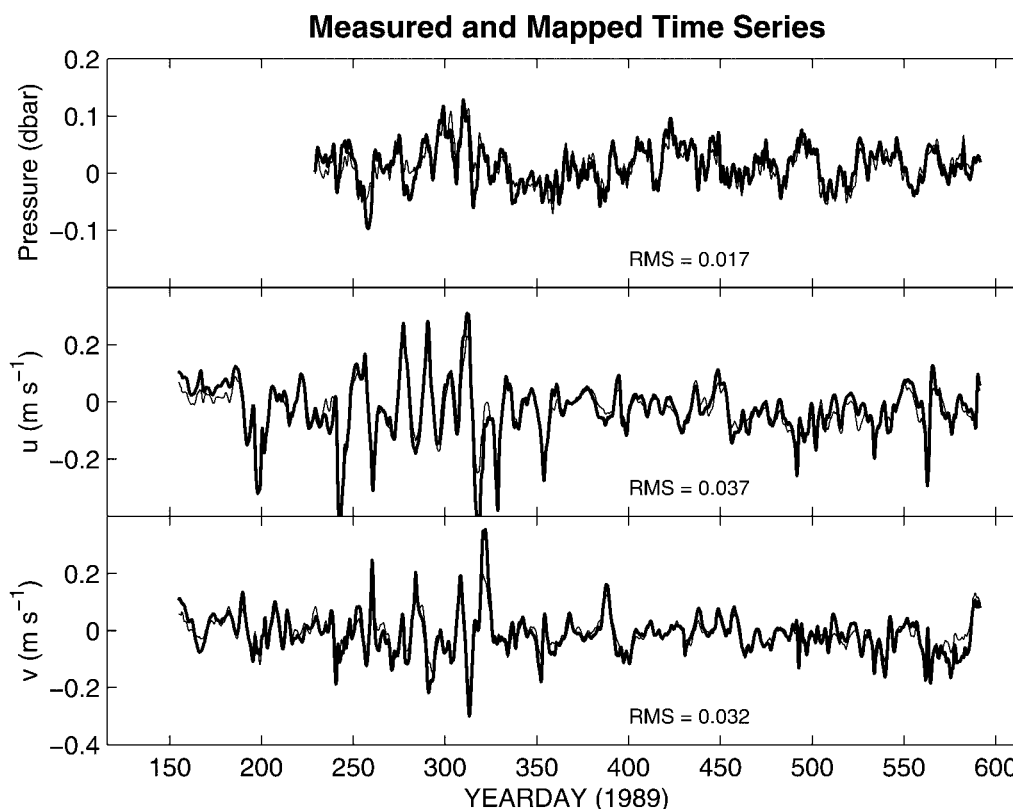


FIG. 4. Measured (bold) and mapped (thin)  $P$ ,  $u$ ,  $v$  time series at site H3. Their difference is denoted “mapping error.”

streamfunction at the pressure measurement sites. These mean streamfunction values could then be used as the pressure reference levels.<sup>1</sup>

In essence, the mean geostrophic pressure field determined from current records was used to produce spatially consistent reference pressures for the measured  $P'$ . The sum of a residual pressure record and its reference pressure,  $P(t, s) = P'(t, s) + \Delta_s P_0(s)$ , will be denoted as the leveled pressure record. The only remaining undetermined constant is independent of location and time, that is, a dynamically unimportant constant.

#### b. Multivariate OI mapping

The multivariate mapping step (denoted “pu2p” and “pu2u”) is indicated midway down Fig. 2 and the mathematical details are given in the appendix. The resulting maps are termed “preliminary” because of a refinement, which is described next.

The OI analysis procedure operates with variables

<sup>1</sup> Choosing an alternate reference than G2 would have produced a different constant offset for all the pressure maps, effectively a hydrostatic offset with no change in the dynamic current fields. Gappy data could have necessitated another approach to determine the best reference offsets from periods of overlapping good data. Fortunately our dataset had few data gaps, so the choice of reference site has no substantial effect upon our mapped fields.

that all have zero mean. Consequently, it is best to first remove a mean field from the input data and subsequent to the OI, to restore a consistent mean to the output. The preliminary maps were generated assuming that the means were zero. Although the mean pressures differed by less than 0.08 db between sites, there was a discernible spatial distribution to the means. Accordingly, the 26-month-long temporal mean pressure field and its corresponding geostrophic velocity were calculated from the maps produced during the preliminary pass of the multivariate OI (Fig. 2). Then, the means were subtracted from the leveled pressure and current records. Next, the OI procedure was applied to the “demeaned” records to produce residual fields. Last, the mean fields were restored to produce the final sequence of pressure and current maps. A result of improving the mean field specification is that the final maps exhibited less smoothing than the preliminary versions.

The preliminary OI step was used only for finding averages of currents or pressures. The results are not particularly sensitive to the choice of correlation length  $r_0$  and the noise-to-signal ratio  $\mathcal{E}_0$  for the OI mapping (defined in appendix), which we chose for this step to be 150 km and 0.05, respectively. These long correlation and low noise values are appropriate for mapping the average fields. For the final OI step, in which the eddy residual pressure and current fields were mapped, the

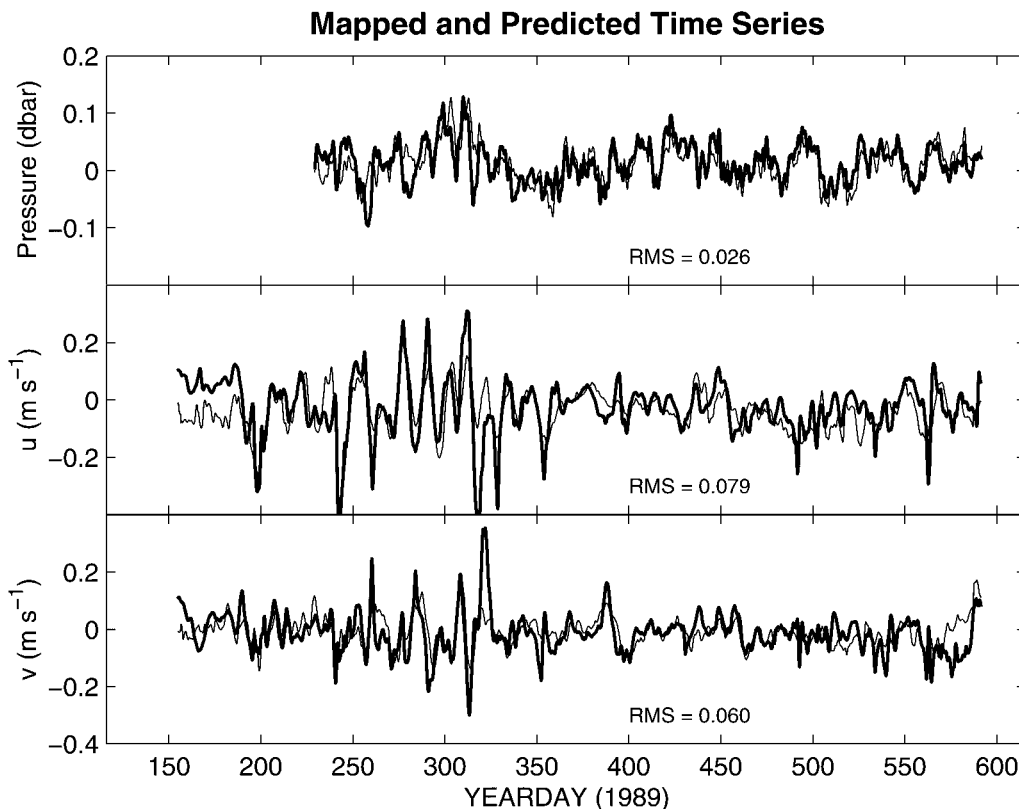


FIG. 5. Measured (bold) and predicted (thin)  $P$ ,  $u$ ,  $v$  time series at site H3. Their difference is denoted “prediction error.”

value for  $r_0$  was chosen by least squares fitting a Gaussian function to the spatial correlation function estimated from the residual data. The value for  $\mathcal{E}_0$  was determined from the estimated uncertainty in the measured data and their residual variance (Qian and Watts 1992). We found  $r_0 = 90$  km and  $\mathcal{E}_0 = 0.10$ , as are appropriate for the shorter correlation lengths and smaller signal levels in the residual eddy fields.

Mathematically, the OI procedure also assumes that the input data have spatially isotropic correlation functions with spatially uniform variance. Even though the observed variance was not uniform, the pressure and current data were not scaled by a variance field for two reasons. First, nonuniformly scaled pressure and current data would no longer be in geostrophic balance, resulting in much more complex cross-covariance functions between pressure and current. Second, the root-mean-square (rms) current speeds at different sites range only from 3 to 9  $\text{cm s}^{-1}$ ; thus scaling by the local variance should not be necessary. In any case, Watts et al. (1989) found that even in the upper-layer jet, where nonuniform variance was more clearly evident, the mapped fields were not particularly sensitive to this prescaling.

The appendix explains further mathematical details and presents the covariance functions that were fitted to the data. The OI procedure is fully documented in Qian and Watts (1992).

### 5. Accuracy verification

The quality of the final maps was evaluated by comparing the pressures and currents derived from the maps and those from measurements. One test was simply a self-consistency check in which the rms differences between the mapped variables and the measured ones were calculated. The other test was similar to the first except that the OI mapped currents and pressures were recalculated excluding the input of either  $P$  or  $(u, v)$  from each site, one at a time. This second test has been performed for all sites but is illustrated here only for site H3. The error from the first test will be designated as “mapping error,” and the error from the latter “prediction error.”

Figure 3 shows mean 3500-m pressure maps for two 1-yr periods, with both the measured and mapped mean current vectors superimposed. Measured vectors are only shown for the sites where the measurements spanned the complete averaging period. The evident good agreement between input and output variables is not only a measure of the self-consistency of the OI, but an indication of the success of the leveling. Note that the mean fields for these particular 1-yr time periods were not forced to be equal by the procedure of leveling the pressure sensors. The rms difference in mapped versus measured velocities and pressures is  $(\overline{\delta u^2})^{1/2} = 2.6$



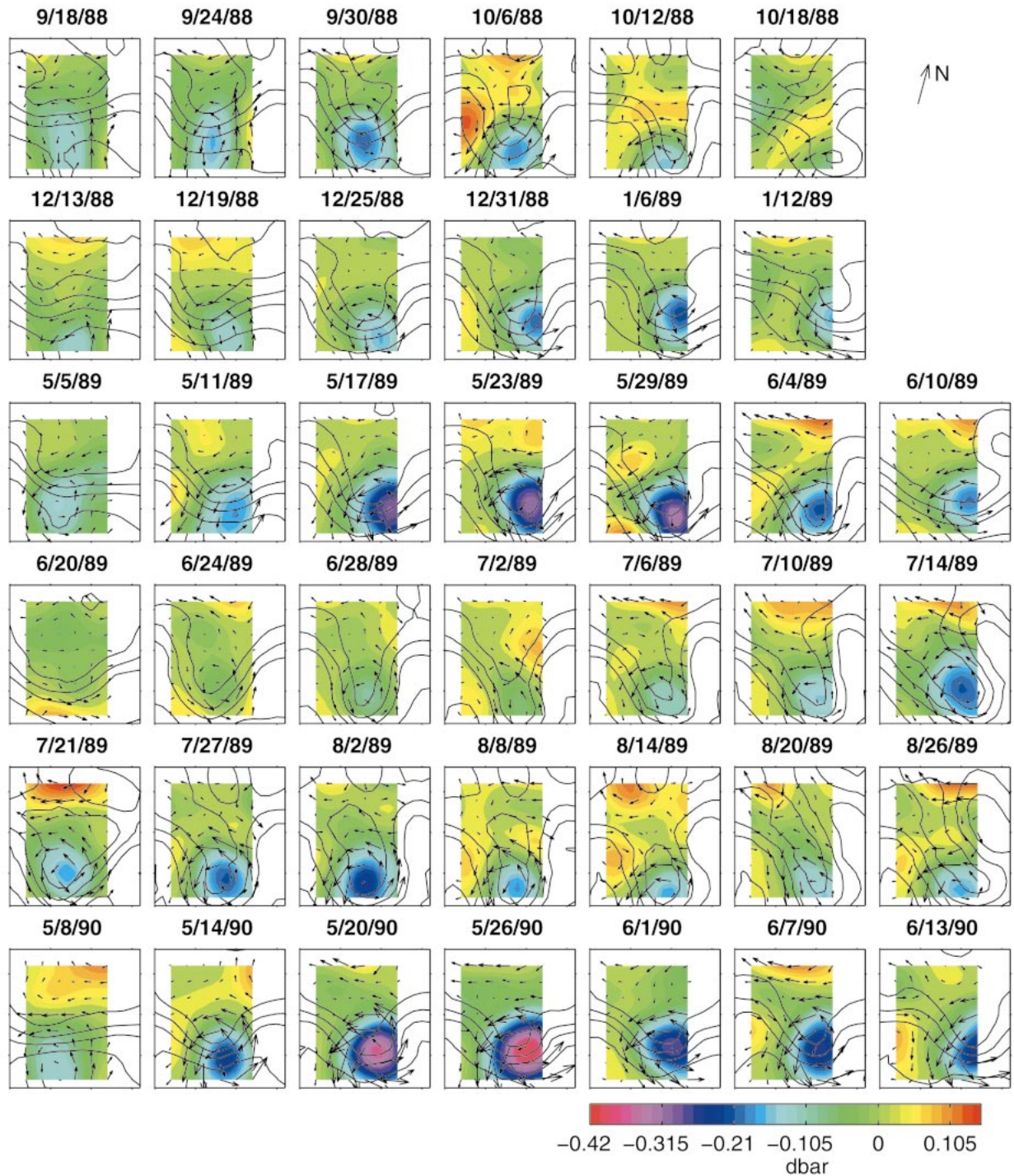


FIG. 6. Plan-view maps of the 3500-m pressure field  $P$  (color-coded, 0.015-db intervals), and the upper jet  $12^{\circ}\text{C}$  main-thermocline depth (solid contours, 200-m interval). The OI-mapped velocities are shown by the vectors where the scale of  $0.25\text{ m s}^{-1}$  is indicated by the compass arrow. Each row illustrates a single steep meander trough event. The maps are for 1200 UTC on the date indicated. Each frame corresponds to the larger box in Fig. 1 and the color-shaded region to the smaller box.

$\text{cm s}^{-1}$ ,  $(\overline{\delta v^2})^{1/2} = 2.2\text{ cm s}^{-1}$ , and  $(\overline{\delta P^2})^{1/2} = 0.019\text{ db}$ , where the overbar indicates an average (weighted by the record lengths) over all sites for both years. These values may be compared with the respective signal stan-

dard deviations,  $\sigma_u = 9.3\text{ cm s}^{-1}$ ,  $\sigma_v = 8.4\text{ cm s}^{-1}$ , and  $\sigma_p = 0.065\text{ db}$ .

Time series of the measured and mapped  $P$ ,  $u$ ,  $v$  are illustrated in Fig. 4 for site H3 and their differences are

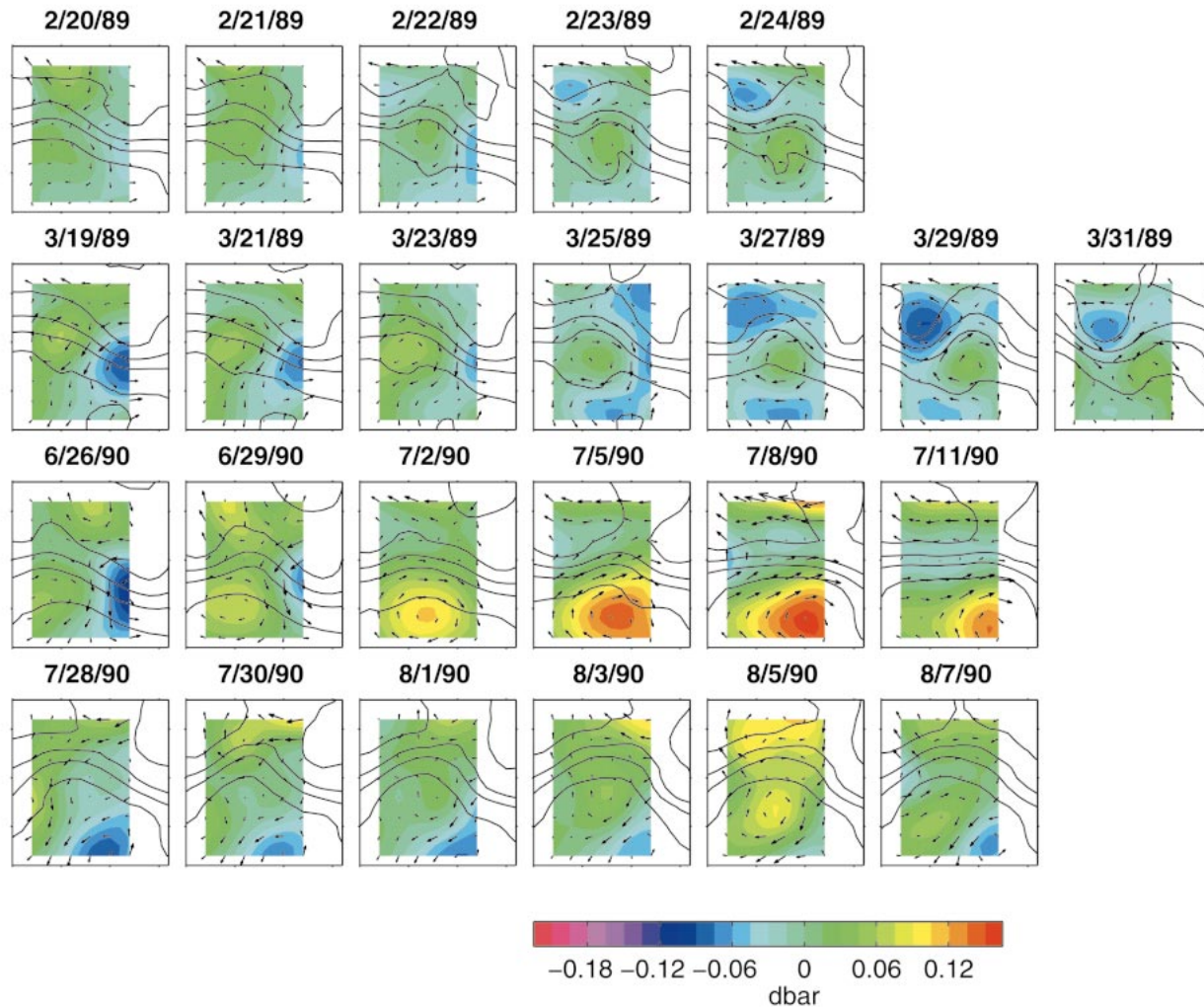


FIG. 7. As in Fig. 6 except showing four meander crest events.

“Mapping Error.” This site was in the northern-central part of the SYNOP array as indicated in Fig. 1. Careful examination reveals that the mapped estimates tend to have peaks that are lower than those of the measurements, because OI is a smoothing process. Nevertheless, the mapped and measured records agree within 0.02 db for pressure and within about 3 cm s<sup>-1</sup> for currents. The correlation coefficients (*r*) between mapped and measured records at site H3 are 0.87, 0.94, and 0.91, respectively, for *P*, *u*, and *v*, respectively.

Times series of the measured and predicted *P*, *u*, *v* are illustrated in Fig. 5 for the same site. The predicted estimates tend to have peaks that are much lower than those of the measurements, which is not surprising since they were interpolated over a large data gap. The correlation coefficients between predicted and measured records at site H3 are 0.71, 0.63, and 0.55 for *P*, *u*, and *v*, respectively. Because site H3 was surrounded by other measurement sites, the prediction error is, in essence, an indicator of the real mapping error

in the regions between the other sites. However, removing the *P* or (*u*, *v*) measurement at H3 as an input to the mapping created a gap between input sites that was twice as large as what actually existed between the full set of measurement sites. Therefore, the prediction error should be substantially worse than the actual mapping error in the areas between the measurement sites. Specifically, the artificial 120-km gap is greater than the eddy correlation length of 90 km used in the OI mapping whereas the measurement spacing is usually smaller, about 60 km. In fact, of all the comparisons made (Qian and Watts 1992) the mapping and prediction errors illustrated on H3 were among the poorest of the cases.

### 6. Examples

We now illustrate several cases in which the spatially and temporally evolving structure of the abyssal pressure and current fields is shown in relationship to the



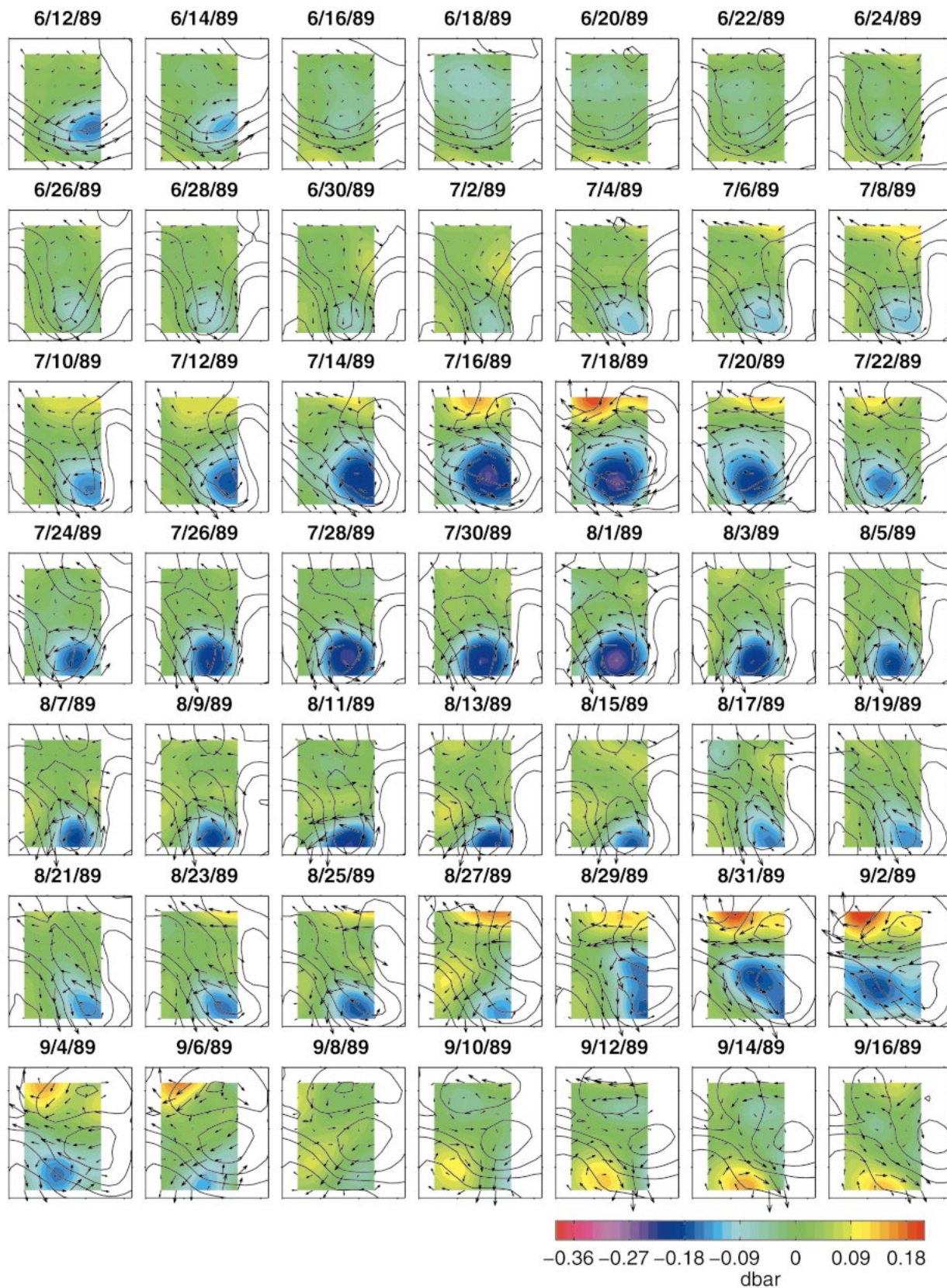


FIG. 8. Similar to Fig. 6 except showing a time sequence of maps at 2-day intervals between Jun and Dec 1989.



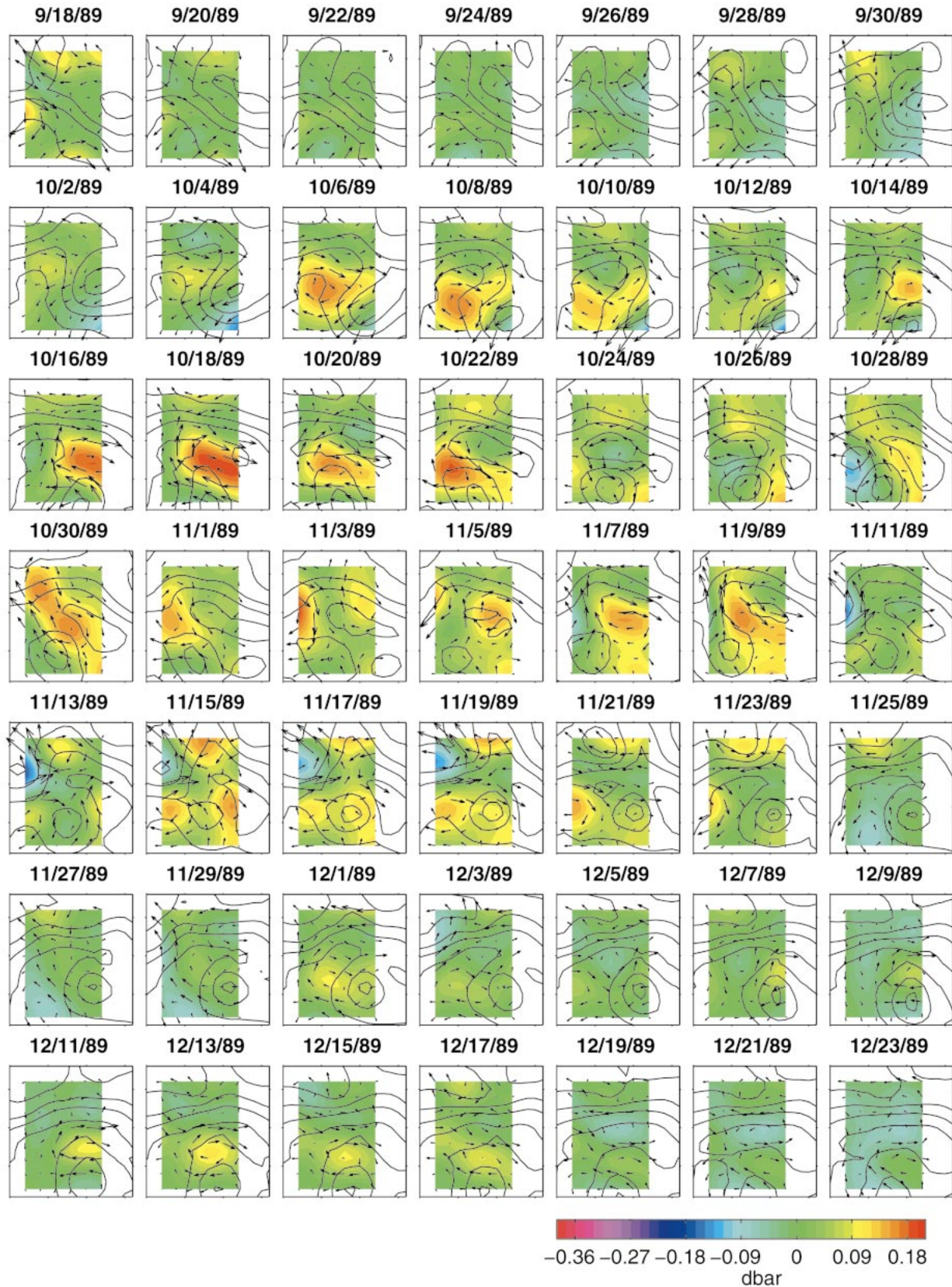


FIG. 8. (Continued)

developing upper Gulf Stream jet. The goal of this section is to highlight the advantages of mapping both the upper and lower layers simultaneously. Other papers (Lindstrom et al. 1997; Howden and Watts 1999; Savidge and Bane 1999b) have discussed the dynamics of the Gulf Stream during these events. We present a suite of time periods for which the mapped fields elucidate the organization of the deep eddy fields associated with meandering of the upper jet.

Deep pressure and current fields mapped at 3500 db using the multivariate OI technique are shown in Figs. 6–8. In these figures, each frame corresponds to the larger boxed region in Fig. 1 and the colored region to the smaller box. The mapping grid was rotated  $15^\circ$  so that the base of each frame points along  $075^\circ$  true. The mapped deep pressure field is color-coded with warmer hues (reds and yellows) indicating higher pressures and cooler hues (blues and magentas) indicating lower pressures. The vectors indicate the multivariate-OI-mapped deep currents. Superimposed on these deep fields are contours of the depth of the main thermocline ( $12^\circ\text{C}$  isotherm depth) as mapped by inverted echo sounders (Tracey and Watts 1991; Watts et al. 1995). Each row in Figs. 6 and 7 corresponds to a different event; the time interval between the frames varies with each event. The two-page Fig. 8 illustrates the full 6-month period from June to December 1989 at 2-day intervals.

#### *a. Abyssal cyclone developing under a steep upper-jet trough*

The most energetic features observed in the mapped fields were intense cyclonic circulations around deep low pressure (LP) centers. These strong cyclones only occurred when steep meander troughs formed in the upper jet. This was not the first time that strong deep currents were observed under the Gulf Stream. Luyten (1977) measured currents in excess of  $0.3\text{ m s}^{-1}$  in the Rise Array near  $70^\circ\text{W}$ . He also mapped the deep stream-function fields, which revealed eddylike circulations. However, their relationship to the upper jet went unrecognized.

Six events are illustrated in Fig. 6. In all the events the deep pressure field and the upper jet developed simultaneously. Each event began with a small-amplitude meander in the upper layer and a weak LP cell in the lower layer. Over the next 2–3-week-period, the upper meander trough amplified and stalled within the array and the deep LP center intensified. During the development phase, the center of the deep cyclone was shifted offshore and slightly ( $\sim 1/8$  wavelength) downstream of the upper trough, a characteristic signature of baroclinic instability. At the peak of development the currents in the cyclones reached maximum speeds of about  $0.45\text{ m s}^{-1}$ . Because the deep currents were organized around the cyclones, the deep flow was not always aligned with the upper flow in an equivalent barotropic sense. Instead, significant cross-frontal flow is readily observed

in Fig. 6 during all six events. The ultimate fate of each event varied, with some of the events leading to ring pinch-off and other events relaxing after upper- and lower-layer centers became more aligned.

Similarities in the evolution of trough axis were observed in all six events. At the initial stage of development, the meander trough axis was typically oriented in a north–south direction. During the intensification phase the trough axis rotated counterclockwise slightly (about  $15^\circ$ ), with the deep LP center remaining phase shifted from the upper trough center. Subsequently, the trough axis continued rotating counterclockwise as the deep LP center propagated downstream. As an example, nearly  $50^\circ$  rotation was observed between 24 June and 14 July 1989.

Several of these trough events have been examined more extensively in other papers. Shay et al. (1995) provide a description of the development of the May 1989 trough event. Lindstrom et al. (1997) focus on the September 1988 event in their examination of vertical motion in the Gulf Stream during meandering events. For their analysis, the mapped fields at several levels were used to diagnose vertical motion via the heat equation. Howden and Watts (1999) describe jet streaks observed flanking the trough axis during both the September and December 1988 events. He et al. (1998) demonstrated that the *baroclinic* shear structure is aligned vertically (i.e., to good approximation “equivalent barotropic”); however the deep *barotropic* reference velocity may be turned (veered or backed) across the baroclinic front (Watts et al. 1995). Savidge and Bane (1999a) provide a general description of the deep cyclones, characterizing such parameters as cyclone movement and swirl and radial velocities as functions of distance from the LP center. Additionally, by examining the available upper-level current measurements together with these maps of the deep fields, Savidge and Bane (1999a) demonstrate clearly the low pressure cells are essentially barotropic. Thus, the position of the deep cyclone relative to the baroclinic front allows a good estimate of the total vertical structure of the current.

#### *b. Abyssal anticyclones propagating under steep upper-jet crests*

Well-developed anticyclonic circulations and high pressure (HP) cells were also observed in the deep fields, however they did not exhibit the same intensity as the cyclones. The anticyclones accompanied large amplitude crests as they propagated rather quickly through the array (Fig. 7). During these events, the centers of the deep anticyclones were aligned with or slightly south of the thermocline expression of meander crest. Unlike the trough events no downstream phase offset was observed. In addition to these HP cells below the crests, in the two 1989 events shown in Fig. 7, deep LP cells accompanied the trailing (rapidly propagating) meander



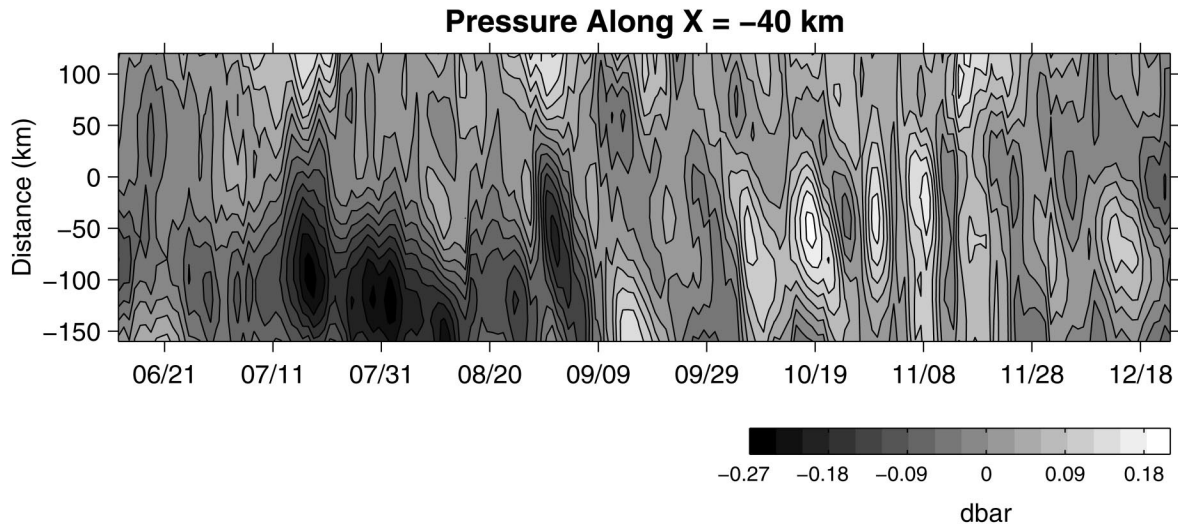


FIG. 9. Time–distance plot of pressure along an approximate N–S slice through the array.

troughs. During these two events, when the crest was centered within the mapping array, the deep currents associated with the anticyclone/cyclone pair were aligned with the baroclinic front in a nearly equivalent barotropic fashion. However, at other times the deep flows exhibited significant cross-frontal components.

The meander crests exhibited relatively little growth in the region. Nevertheless, during the 2-yr field program 2 or 3 warm core rings were observed to pinch off just along the eastern edge of the mapping array. However, these rings resulted from the steepening of meander troughs rather than crests. After the formation of the steep trough, the path was distorted into an “S” pattern and ultimately a ring pinched off from the downstream northern loop (see Fig. 8). It seems likely that the topographic slope, which is much steeper to the north than to the south in this region, may inhibit meander crest growth.

During the Summer 1990 (Fig. 7), strong deep anticyclones developed within the array. However, during both of these events the general path of the Gulf Stream both east and west of our mapping region (as revealed in AVHRR images) was south of its temporal mean position and only a fraction of each crest was within the mapping array. For example, on 8 July, only the peak of the crest was within the array, giving the impression that the path was relatively straight. The strength of the deep anticyclonic flow (maximum speeds of  $0.30 \text{ m s}^{-1}$ ) suggested otherwise and satellite imagery confirmed the existence of the broad meander crest.

The March 1989 crest event has been examined in greater detail by Shay et al. (1995), Lindstrom et al. (1997), and Howden and Watts (1999).

### c. Ring–stream interactions and TRWs

Figure 8 shows a 6-month period when both the upper and lower layers exhibited complex features that

evolved over time. (Embedded within this interval are two steep trough development events from Fig. 6, but the focus now is on the energetic events after they matured.) During this period the path of the upper baroclinic jet transitioned from a steep trough, to a distorted “S” path, to a relative straight path with an associated cold core ring. Both warm (WCR) and cold core (CCR) rings pinched off and subsequently interacted with or reattached to the main jet. Simultaneous with these events in the upper layer, strong cyclonic and anticyclonic flows were observed in the deep fields and a set of propagating deep eddies passed through the region. Propagation of the features in the deep fields was typically to the southwest throughout this period, unlike the bulk of the 2-yr observational period when eastward propagation was prevalent.

Twice during the period from early July through early September 1989 the Gulf Stream path was distorted from steep trough to an S-shaped path and a WCR was shed from the downstream loop. The joint spinup of the upper and lower cyclones and the rotation of the trough axis (as previously described) can be tracked in Fig. 8. In addition, the maps reveal that as the upper jet path distorted into an S shape strong westward currents ( $0.3 \text{ m s}^{-1}$ ) occurred in the northern part of the array. These currents appear to be organized around an anticyclonic HP cell rather than being associated with the Deep Western Boundary Current. The deep anticyclone is shifted to the north and west of the upper-layer crest or loop.

Figure 8 shows that distortion of the upper jet continued through the early fall until a CCR ring was shed in mid-October. The ring translated quickly westward and reattached to the Gulf Stream in late October. Subsequently, the CCR moved eastward while remaining attached to the jet. By late November the CCR once again separated. However, during this period there was no obvious relationship between the upper jet and the



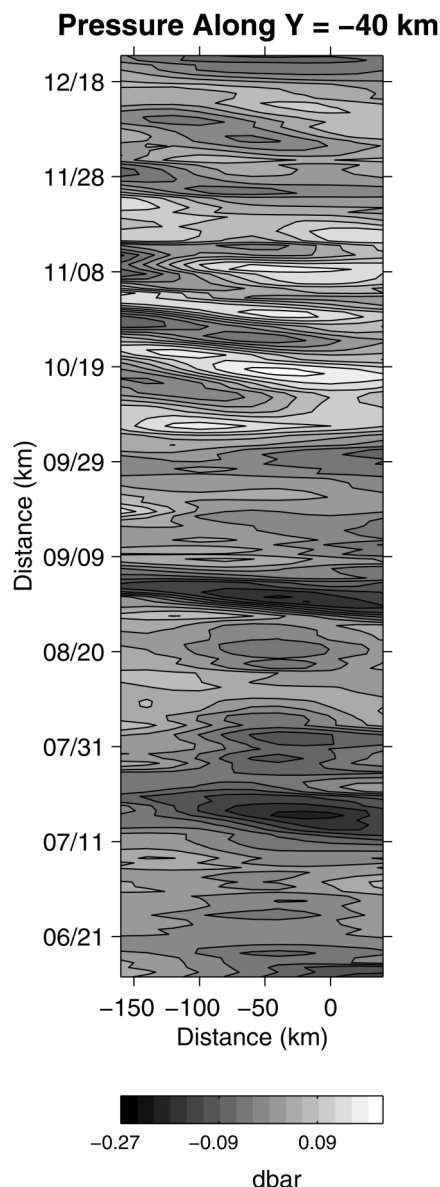


FIG. 10. Time–distance plot of pressure along an approximate E–W slice through the array. The color bar and contour interval are identical to those in Fig. 9.

deep pressure and current fields. Instead, a set of weak-to-moderate high and low pressure centers propagated quickly through the array.

Figures 9 and 10 illustrate the phase propagation of these pressure centers. Figure 9 plots the deep pressure field along a top-to-bottom section through the array versus time and Fig. 10 a left-to-right section. (Recall that the orientation of the mapping region results in these sections being rotated  $15^\circ$  counterclockwise from true E–W and N–S.) The deep eddies appear in these figures as the series of high and low pressure cells between early October and mid-November. The predominantly westward propagation of the eddies is clearly evident

in Fig. 10 and the southerly component is evident for some individual eddies in Fig. 9. In general, the eddies tended to transit through the array progressively farther to the north. From Figs. 9 and 10 propagation speeds of  $20\text{--}30\text{ km day}^{-1}$  and periods of 10–15 days were estimated for these eddies. These properties are consistent with topographic Rossby waves (TRWs). Because these eddies appeared within the array at nearly the same time that the CCR initially separated from the Gulf Stream, it is possible that either (i) they originated somewhere to the east and were instrumental in initiating the pinching-off process or (ii) they were radiated by the ring formation process.

Southwestward propagation is also evident in Figs. 9 and 10 during the middle of July and late August/early September. Figure 8 shows that during both of these periods strong cyclonic flow was present in the deep layer and the upper trough axis rotated substantially. Closer examination of the latter event reveals that the cyclone had two distinct centers. Both centers are visible in the maps for 29 and 31 August. One center, located at the bottom right, appears to be aligned with the center of the steep trough. This center propagated eastward out of the array. The second center entered the array near the midpoint along the eastern edge on 27 August. It translated to the south and west, reaching the lower left corner by 4 September. This process resulted in the LP center shifting from the eastern portion of the array to the western portion. It is interesting to speculate that a similar process was also responsible for the westward shift of the deep cyclone between 12 and 22 July. Although two distinct LP centers are not apparent in Fig. 8 during that period, the cyclone greatly intensified between the two dates and a small bulge at the northeastern edge of the cyclone rotated to the southwest.

## 7. Summary

This paper documents how daily maps of the abyssal pressure and current fields beneath the Gulf Stream were generated with temporally and spatially consistent leveling. Leveling is a technique used to reference all measurements onto the same geopotential surface. Here, the pressures were leveled by independently measuring the abyssal currents and assuming their mean fields were geostrophic and depth independent. While streamfunction maps could have been generated from either dataset alone, there is considerable advantage in combining the two. Maps generated from coherently spaced current meter data would have been spatially consistent, however the pressure reference level would vary for each map. Conversely, pressure records have a temporally consistent reference, which varies from site to site. By combining the two measurements in a multivariate mapping procedure spatially and temporally consistent maps were obtained. Additionally, specifying both the pressure and its gradient as inputs resulted in maps with significantly reduced errors. The mapped abyssal pres-

sure and current fields had typical mean square errors of only 0.0005 db<sup>2</sup> and 4 cm<sup>2</sup> s<sup>-2</sup>.

These maps of the abyssal pressure and current fields have been highly informative to the understanding of the dynamical structure of the deep field beneath the Gulf Stream. Repeatedly throughout the 2-yr observation program, abyssal flows were found to be organized into strong cyclonic and anticyclonic circulations. The eddies were observed to intensify jointly with developing steep troughs and crests in the upper baroclinic jet. The existence of organized cyclones and anticyclones with flows of 0.3–0.45 m s<sup>-1</sup> has fundamentally altered the synoptic view of the Gulf Stream as a rigid structure that merely shifts laterally. Examination of the upper and deep fields together revealed that although the two fields can sometimes be aligned in an equivalent barotropic fashion, significant cross-frontal flows were commonplace.

*Acknowledgments.* This research program has been sponsored by the Office of Naval Research under Contracts N00014-90J-1568 and N00014-97-10138 and the National Science Foundation under Grants OCE87-17144 and OCE93-14581.

APPENDIX

Multivariate OI Correlation Functions

The OI procedure, adapted from (Bretherton et al. 1976), has the goal to map pressure  $P$  and velocity ( $u, v$ ) from limited observations with noise, and constrained, in this study, to satisfy geostrophic balance. The best linear combination of input measurements,  $\phi$  (which in our case is multivariate,  $P, u,$  and  $v$  on measurement sites), is sought to estimate the physical variable,  $\theta$  (which may also be either  $P, u,$  or  $v,$  on any location within or near the measurement array), taking into account statistical cross-covariance properties between the variables. This can be expressed as

$$\hat{\theta} = \sum_{s=1}^N b_s \phi_s = \mathbf{b}^T \phi,$$

where the weights,  $\mathbf{b}$ , at  $N$  input sites (labeled  $s = 1, \dots, N$ ) are selected to minimize the expected error,

$$\mathcal{E} = E\{(\hat{\theta} - \theta)^2\}.$$

Here  $\theta$  and  $\phi$  are assumed to be random variables with zero mean;  $E\{ \}$  denotes the expectation value operator. The result, which may be termed the Gauss–Markov theorem, is

$$\hat{\theta} = \mathbf{C}\mathbf{A}^{-1} \phi,$$

where  $\mathbf{b} = \mathbf{C}\mathbf{A}^{-1}$ , and  $\mathbf{A} = E\{\phi\phi^T\}$  is the covariance matrix between inputs, with elements  $A_{sr} = E\{\phi_s\phi_r\}$ , and  $\mathbf{C} = E\{\theta\phi^T\}$  is the cross-covariance row-vector between the output variable and each of the inputs, with elements  $C_r = E\{\theta\phi_r\}$ . The error field is

$$\mathcal{E} = E\{\theta^2\} - \mathbf{C}\mathbf{A}^{-1}\mathbf{C}^T.$$

The weights  $\mathbf{b}$  and the errors  $\mathcal{E}$  are determined entirely from the statistics, that is, based on the covariances as a function of only the measurement locations.

An important property of the above linear estimator is that the optimal estimate of a linear operator  $\mathcal{L}$  on  $\theta$  may be found by applying the operator on the the optimal estimate of  $\theta$ ; that is,

$$\hat{\theta}_{\mathcal{L}} = \mathcal{L}_{\mathbf{x}}[\hat{\theta}(\mathbf{x})].$$

It follows that  $\hat{\theta}_{\mathcal{L}}$  can be found from the *same* input data by applying the linear operator to the covariance vector (i.e., simply by redefining the covariance function  $\mathbf{C}$ , as follows <sup>A1</sup>:

$$\begin{aligned} \hat{\theta}_{\mathcal{L}} &= \mathcal{L}_{\mathbf{x}}[\hat{\theta}(\mathbf{x})] = \mathcal{L}_{\mathbf{x}}[\mathbf{C}(\mathbf{x}, \mathbf{y})\mathbf{A}^{-1}(\mathbf{y}_1, \mathbf{y}_2)\phi(\mathbf{y})] \\ &= \mathbf{C}_{\mathcal{L}}\mathbf{A}^{-1}\phi. \end{aligned}$$

Hence the new cross-covariance function to estimate  $\hat{\theta}_{\mathcal{L}}$  is

$$\mathbf{C}_{\mathcal{L}} \equiv E\{\mathcal{L}_{\mathbf{x}}[\theta(\mathbf{x})]\phi^T(\mathbf{y})\} = \mathcal{L}_{\mathbf{x}}[\mathbf{C}(\mathbf{x}, \mathbf{y})]. \quad (\text{A1})$$

As an example of using this extension, the geostrophic constraint may be imposed *via* the covariance functions. If we let  $\theta$  be the velocity component  $u$  or  $v$ , and  $\phi$  be pressure  $P$ , the mapping is from pressure to velocity (designated “p2u”). The linear operators for the above formulas are defined from  $\mathbf{u} = -(1/f\rho)\partial_y\phi = \mathcal{L}^u\phi$ , or  $\mathbf{v} = (1/f\rho)\partial_x\phi = \mathcal{L}^v\phi$ . So the proper shorthand expressions for mapping p2u are

$$\hat{\mathbf{u}} = (\mathcal{L}^u\mathbf{C})\mathbf{A}^{-1}\phi \quad \hat{\mathbf{v}} = (\mathcal{L}^v\mathbf{C})\mathbf{A}^{-1}\phi.$$

Note that these estimated  $\hat{\mathbf{u}}$  and  $\hat{\mathbf{v}}$  *exactly* satisfy the geostrophic constraint regardless of the noise in the input data  $\phi$  on which they depend, since the algorithm is equivalent to first estimating a streamfunction and then applying  $\mathcal{L}^u$  and  $\mathcal{L}^v$  on it.

A related fact is that the covariance function between outputs,  $\mathcal{L}_{\mathbf{y}_1}[\eta(\mathbf{y}_1)]$  and  $\mathcal{L}_{\mathbf{y}_2}[\xi(\mathbf{y}_2)]$ , of two linear operators<sup>A2</sup> can be found by applying the two operators to the covariance function between two input variables,  $\eta(\mathbf{y}_1)$  and  $\xi(\mathbf{y}_2)$ . This can be expressed as

$$\begin{aligned} E\{\eta_{\mathcal{L}_{\mathbf{y}_1}}\xi_{\mathcal{L}_{\mathbf{y}_2}}\} &= E\{\mathcal{L}_{\mathbf{y}_1}\eta(\mathbf{y}_1)\mathcal{L}_{\mathbf{y}_2}\xi(\mathbf{y}_2)\} \\ &= \mathcal{L}_{\mathbf{y}_1}\mathcal{L}_{\mathbf{y}_2}E\{\eta(\mathbf{y}_1)\xi(\mathbf{y}_2)\}. \end{aligned} \quad (\text{A2})$$

<sup>A1</sup> Here the different position variable names inside the parentheses are used to distinguish the position variables associated with different physical variables. For example,  $\theta(\mathbf{y}_2)$  indicates that the matrix element  $\phi_s$  depends on a position (site) variable  $\mathbf{y}_2$ ;  $\mathbf{A}(\mathbf{y}_1, \mathbf{y}_2)$  indicates that the matrix element  $A_{rs} = E\{\phi_r(\mathbf{y}_1)\phi_s(\mathbf{y}_2)\}$  depends on two position variables  $\mathbf{y}_1, \mathbf{y}_2$  associated with  $\phi_r$  and  $\phi_s$ , respectively. The subscript of the operator is also used to indicate its dependent variable.

<sup>A2</sup> The notation  $\mathcal{L}_{\mathbf{y}_1}$  and  $\mathcal{L}_{\mathbf{y}_2}$  is meant to imply two different operators operating on different variables. It is usually clear from the context whether the two operators are the same or different, so this notation avoids introducing more complicated symbols to indicate a different linear operator.

TABLE A1. Covariance functions of streamfunction and current. Here  $\alpha_x$  and  $\alpha_y$  are defined respectively by  $x_2 - x_1 = r \cos \alpha_x$  and  $y_2 - y_1 = r \cos \alpha_y$ .

	$\psi(x_2, y_2)$	$u(x_2, y_2)$	$v(x_2, y_2)$
$\psi(x_1, y_1)$	$F(r) = \sigma_\psi^2 \exp\left(-\left(\frac{r}{r_0}\right)^2\right)$	$(r \cos \alpha_x) 2r_0^{-2} F(r)$	$-(r \cos \alpha_y) 2r_0^{-2} F(r)$
$u(x_1, y_1)$	$-(r \cos \alpha_x) 2r_0^{-2} F(r)$	$\left[1 - 2\left(\frac{r}{r_0}\right)^2 \cos^2 \alpha_x\right] 2r_0^{-2} F(r)$	$\left[2\left(\frac{r}{r_0}\right)^2 \cos \alpha_x \cos \alpha_y\right] 2r_0^{-2} F(r)$
$v(x_1, y_1)$	$(r \cos \alpha_y) 2r_0^{-2} F(r)$	$\left[2\left(\frac{r}{r_0}\right)^2 \cos \alpha_x \cos \alpha_y\right] 2r_0^{-2} F(r)$	$\left[1 - 2\left(\frac{r}{r_0}\right)^2 \cos^2 \alpha_y\right] 2r_0^{-2} F(r)$

Note Eq. (2) is a special case of the above relation where  $\mathcal{L}_{y_2}$  is an identity operator.

For the present study, a Gaussian covariance function was fitted to the observed pressure data

$$E\{P(x_1, y_1)P(x_2, y_2)\} = \sigma_p^2 \exp(-r^2/r_0^2),$$

where  $\sigma_p^2$  is the pressure variance,  $r = [(x_1 - x_2)^2 + (y_1 - y_2)^2]^{1/2}$ , and  $r_0$  is a chosen correlation length. For convenience, we define a streamfunction  $\psi = P/f\rho$ . The autocovariance function of  $\psi$  is then

$$E\{\psi(x_1, y_1)\psi(x_2, y_2)\} = \sigma_\psi^2 \exp(-r^2/r_0^2). \quad (\text{A3})$$

Table A1 lists all the relevant covariance functions that are determined using Eqs. (A2) and (A3). As an example,  $E\{u(x_1, y_1)v(x_2, y_2)\}$  in matrix **A** needed for mapping from velocity to pressure (designated u2p) can be found by

$$\begin{aligned} & E\{u(x_1, y_1)v(x_2, y_2)\} \\ &= E\left\{-\frac{\partial\psi(x_1, y_1)}{\partial y_1} \frac{\partial\psi(x_2, y_2)}{\partial x_2}\right\} \\ &= -\frac{\partial}{\partial y_1} \frac{\partial}{\partial x_2} E\{\psi(x_1, y_1)\psi(x_2, y_2)\} \\ &= 4(x_2 - x_1)(y_2 - y_1)r_0^{-4}\sigma_\psi^2 \exp(-r^2/r_0^2). \end{aligned}$$

Note that the constant  $\sigma_\psi^2$  appears in the numerator and denominator of the product  $\mathbf{CA}^{-1}$ , thus canceling out. Hence it is conventional to work with normalized covariance functions, treating  $\sigma_\psi^2 = 1$ .

In the last paragraph as well as in Table A1, we did not take into account the noise in the measurements. We now assume that the noise at a measurement site is neither correlated with measured signals nor with the noise at other measurement sites. Thus, the noise contribution appears only on the diagonal entries of the matrix **A**. Specifically, if **A**<sub>0</sub> is the matrix whose elements are derived from the entries in Table A1, then the covariance matrix between inputs is

$$\mathbf{A} = \mathbf{A}_0 + \mathcal{E}_0,$$

where  $\mathcal{E}_0$  is a diagonal matrix whose *s*th diagonal el-

ement is the noise variance in the *s*th input variable. Note the matrix **C** will not be affected by the noise because of the assumption that the noise in the input is not correlated with the output signal.

#### REFERENCES

- Baker, D. J., 1981: Ocean instruments and experimental design. *Evolution of Physical Oceanography*, B. A. Warren and C. Wunsch, Eds., The MIT Press, 396–433.
- Bretherton, F. P., R. E. Davis, and C. B. Fandry, 1976: A technique for objective analysis and design of oceanographic experiments applied to MODE-73. *Deep-Sea Res.*, **23**, 559–582.
- Cronin, M., and D. R. Watts, 1996: Eddy-mean flow interaction in the Gulf Stream at 68°W. Part I: Eddy energetics. *J. Phys. Oceanogr.*, **26**, 2107–2131.
- Fields, E., and D. R. Watts, 1990: The SYNOP Experiment: Inverted echo sounder data report for Jun 1988 to Sep 1989. G.S.O. Tech. Rep. 90-2, Graduate School of Oceanography, University of Rhode Island, Narragansett, RI, 232 pp. [Available from Pell Marine Science Library, University of Rhode Island, Narragansett, RI 02882.]
- , and —, 1991: The SYNOP Experiment: Inverted echo sounder data report for Jun 1989 to Sep 1990. G.S.O. Tech. Rep. 91-2, Graduate School of Oceanography, University of Rhode Island, Narragansett, RI, 254 pp. [Available from Pell Marine Science Library, University of Rhode Island, Narragansett, RI 02882.]
- Filloux, J. H., 1970: Deep sea tide gauge with optical readout of Bourdon tube rotations. *Nature*, **226**, 936–937.
- , 1980: Pressure fluctuations on the open ocean floor over a broad frequency range: New program and early results. *J. Phys. Oceanogr.*, **10**, 1959–1971.
- He, Y., D. R. Watts, and K. L. Tracey, 1998: Determining geostrophic velocity shear profiles with inverted echo sounders. *J. Geophys. Res.*, **103**, 5607–5622.
- Howden, S. D., and D. R. Watts, 1999: Jet streaks in the Gulf Stream. *J. Phys. Oceanogr.*, **29**, 1910–1924.
- Kim, H.-S., 1994: An equivalent-barotropic data-assimilating model of Gulf Stream meanders. Ph.D. thesis, Graduate School of Oceanography, University of Rhode Island, Narragansett, 93 pp.
- Lindstrom, S. S., and D. R. Watts, 1994: Vertical motion in the Gulf Stream near 68°W. *J. Phys. Oceanogr.*, **24**, 2321–2333.
- , X. Qian, and D. R. Watts, 1997: Vertical motion in the Gulf Stream and its relation to meanders. *J. Geophys. Res.*, **102**, 8485–8503.
- Luyten, J. R., 1977: Scales of motion in the deep Gulf Stream and across the Continental Rise. *J. Mar. Res.*, **35**, 49–74.
- Munk, W. H., and D. E. Cartwright, 1966: Tidal spectroscopy and prediction. *Philos. Trans. Roy. Soc. London*, **259A**, 533–581.

- Paros, J. M., 1976: Digital pressure transducers. *Measurements Data*, **10**, 74–79.
- Pedlosky, J., 1987: *Geophysical Fluid Dynamics*. Springer-Verlag, 710 pp.
- Qian, X., and D. R. Watts, 1992: The SYNOP Experiment: Bottom pressure maps for the central array for May 1988 to August 1989. G.S.O. Tech. Rep. No. 90-2, Graduate School of Oceanography, University of Rhode Island, Narragansett, 187 pp. [Available from Pell Marine Science Library, University of Rhode Island, Narragansett, RI 02882.]
- Savidge, D. K., and J. M. Bane, 1999a: Cyclogenesis in the deep ocean beneath the Gulf Stream: 1. Description. *J. Geophys. Res.*, **104**, 18 111–18 126.
- , and —, 1999b: Cyclogenesis in the deep ocean beneath the Gulf Stream: 2. Dynamics. *J. Geophys. Res.*, **104**, 18 127–18 140.
- Shay, T. J., J. M. Bane Jr., D. R. Watts, and K. L. Tracey, 1995: Gulf Stream flow field and events at 68°W. *J. Geophys. Res.*, **100**, 22 565–22 589.
- Tracey, K. L., and D. R. Watts, 1991: The SYNOP Experiment: Thermocline depth maps for the Central Array October 1987 to August 1990. G.S.O. Tech. Rep. No. 91-5, Graduate School of Oceanography, University of Rhode Island, Narragansett, 193 pp. [Available from Pell Marine Science Library, University of Rhode Island, Narragansett, RI 02882.]
- Watts, D. R., and H. Kontoyiannis, 1990: Deep-ocean bottom pressure measurement: Drift removal and performance. *J. Atmos. Oceanic Technol.*, **7**, 296–306.
- , K. T. Tracey, and A. I. Friedlander, 1989: Producing accurate maps of the Gulf Stream thermal front using objective analysis. *J. Geophys. Res.*, **94**, 8040–8052.
- , J. M. Bane Jr., K. L. Tracey, and T. J. Shay, 1995: Gulf Stream path and thermocline structure near 74°W and 68°W. *J. Geophys. Res.*, **100**, 18 291–18 312.
- Wearn, R. B., and N. G. Larson, 1982: The measurements of the sensitivities and drift of Digiquartz pressure sensors. *Deep-Sea Res.*, **29**, 111–134.